







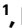



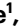








Laser-driven high-energy proton beams from cascaded acceleration regimes

Received: 7 August 2023

Accepted: 5 April 2024

Published online: 13 May 2024

 Check for updates

Tim Ziegler ^{1,2}✉, Ilja Göthel^{1,2}, Stefan Assenbaum ^{1,2}, Constantin Bernert ^{1,2}, Florian-Emanuel Brack ^{1,2}, Thomas E. Cowan ^{1,2}, Nicholas P. Dover ^{3,4}, Lennart Gaus ^{1,2}, Thomas Kluge ¹, Stephan Kraft ¹, Florian Kroll ¹, Josefine Metzkes-Ng ¹, Mamiko Nishiuchi ³, Irene Prencipe¹, Thomas Püschel ¹, Martin Rehwald ^{1,2}, Marvin Reimold ^{1,2}, Hans-Peter Schlenvoigt ¹, Marvin E. P. Umlandt ^{1,2}, Milenko Vescovi ¹, Ulrich Schramm ^{1,2} & Karl Zeil ¹

Laser-driven ion accelerators can deliver high-energy, high-peak current beams and are thus attracting attention as a compact alternative to conventional accelerators. However, achieving sufficiently high energy levels suitable for applications such as radiation therapy remains a challenge for laser-driven ion accelerators. Here we generate proton beams with a spectrally separated high-energy component of up to 150 MeV by irradiating solid-density plastic foil targets with ultrashort laser pulses from a repetitive petawatt laser. The preceding laser light heats the target, leading to the onset of relativistically induced transparency upon main pulse arrival. The laser peak then penetrates the initially opaque target and triggers proton acceleration through a cascade of different mechanisms, as revealed by three-dimensional particle-in-cell simulations. The transparency of the target can be used to identify the high-performance domain, making it a suitable feedback parameter for automated laser and target optimization to enhance stability of plasma accelerators in the future.

Particle accelerators driven by high-intensity lasers have been an area of increasing interest over the last two decades¹, as they can produce beam parameters suitable for a wide range of applications in science, medicine and industry. Of particular interest is the generation of pulsed, high-intensity multi-megaelectron volt ion beams from relativistic plasmas created at laser-irradiated solids^{2,3}. These laser-driven ion beams can be used for multidisciplinary applications including radiation therapy⁴, injectors for advanced accelerator concepts^{5,6}, neutron production⁷ and fast ignition in inertial confinement fusion⁸.

A major focus in this research field is increasing the achievable proton energies, particularly beyond the 100 MeV frontier. Historically, record proton energies were mainly reported from large-scale high-energy (>100 J) lasers with limited shot rate,

irradiating micrometre-thick foil targets and inducing acceleration via hot-electron-driven plasma expansion known as target normal sheath acceleration^{9–11}. The maximum proton energies for this mechanism are primarily enhanced by increasing the amount of laser energy coupled into the plasma, as scaling occurs with the square root of the laser energy¹². Conceptually different acceleration mechanisms drive protons in a more coherent manner to further increase maximum energies with a more favourable scaling^{13–18}. These advanced concepts enabled compact high-intensity lasers with ultrashort pulses to achieve comparable performance levels with substantially reduced laser energy (few joules) and repetition rates relevant for practical applications^{19–22}. Individual mechanisms, as demonstrated in numerical studies under idealized conditions, are difficult to isolate experimentally and can lead

¹Helmholtz-Zentrum Dresden-Rossendorf, Dresden, Germany. ²Technische Universität Dresden, Dresden, Germany. ³Kansai Institute for Photon Science, National Institutes for Quantum Science and Technology, Kizugawa, Japan. ⁴The John Adams Institute for Accelerator Science, Blackett Laboratory, Imperial College London, London, UK. ✉e-mail: t.ziegler@hzdr.de

to potentially ambiguous signatures. The identification of the optimal coupling of mechanisms to effectively exploit the laser-induced acceleration fields thus proved to be complex. Under typical experimental conditions, multiple mechanisms either coexist or cascade sequentially^{23–26}, as evidenced by the recent achievement of near-100-MeV record energies in a hybrid scheme utilizing a high-energy laser²⁷. Here we report experimental results for plasma-accelerated proton beams featuring a spectrally separated high-energy component of up to 150 MeV at application-relevant particle yields. Irradiating solid-density plastic foil targets with ultrashort laser pulses from a repetitive petawatt laser enabled these results without the need for shot-rate-limiting concepts such as cleaning of the temporal laser contrast (for example, with plasma mirrors²⁸) or specialized target treatment (for example, refs. 29,30). By matching the initial target thickness to the laser parameters, multiple shots under optimal conditions resulted in proton acceleration to energies beyond 100 MeV. The preceding laser light heated the target, leading to its subsequent expansion and a near-critical plasma density profile. This permitted the laser main pulse to penetrate the initially opaque target and trigger proton acceleration via a cascade of different mechanisms, as confirmed by three-dimensional (3D) particle-in-cell simulations. The transmitted laser light, which is linked to target transparency, proved to be an easily accessible control parameter for identifying the high-performance domain within the acquired dataset.

Previous research has shown that plasma acceleration can be enhanced when the laser main pulse arrival coincides with the onset of target transparency^{26,27,31–38}, making this a promising way to improve particle beam parameters such as energy and directionality. The moment when the initially opaque target becomes transparent to the laser is termed the onset of relativistically induced transparency (RIT)³⁹ and occurs when the plasma frequency drops below the laser frequency due to the relativistic mass increase of the electrons. Investigating plasma acceleration at the onset of RIT first requires identifying the optimal interaction parameters for the specific laser used.

In a dedicated prestudy, the target thickness was varied over a wide range and the acceleration performance was compared to numerical simulations²⁶. An optimal target thickness between 200 and 300 nm was determined, where electron expulsion from the target bulk due to RIT led to extremely localized space charge fields. These findings provided the basis for the present study, in which the nominal laser and target parameters were not intentionally varied.

A schematic of the experimental setup at the DRACO-PW^{21,40} laser is shown in Fig. 1. Laser pulses (pulse duration ≈ 30 fs) are focused by an $f/2.3$ parabola (peak intensity $\sim 6.5 \times 10^{21}$ W cm⁻²) onto plastic foils of 250 ± 25 nm thickness under oblique incidence (50°), allowing separation of different acceleration components and particle emission directions. A ceramic screen was used to measure the amount of laser light transmitted through the target, helping to analyse the interaction regime for each shot. The generated particle beam was characterized by multiple detectors based on different detection principles to provide robust measurement of the maximum energy (details in Methods). Thomson parabola spectrometers (TPSs) positioned at 15° (TPS15) and 45° (TPS45) with respect to the laser propagation direction (0°) enabled the analysis of particle spectra with high-energy resolution. A time-of-flight (TOF) detector complemented the maximum proton energy detection at 31° (TOF31). A scintillator-based beam profiler equipped with absorbers of different thicknesses at its front provided a spatial measurement of accelerated protons at discrete threshold energies.

A slit in the central horizontal plane of the profiler allowed for the parallel operation of the TPS and TOF detectors. For selected shots, a stack of radiochromic films was inserted to provide an energy-resolved spatial dose distribution of the particle beam. Figure 2a displays the maximum proton energies as a function of transmitted laser light for TPS measurements in the two surveyed spatial directions. Even small

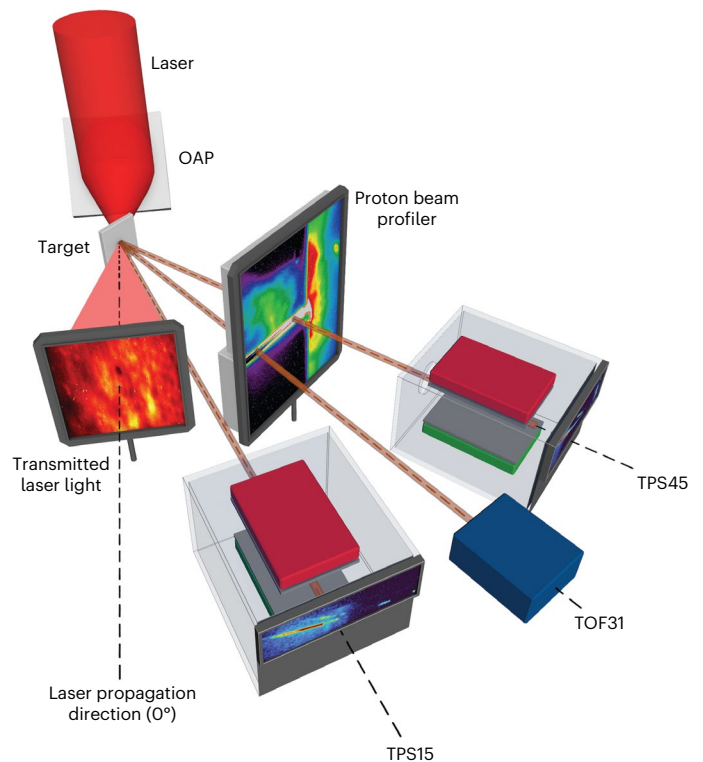


Fig. 1 | Illustration of the experimental setup. Laser pulses are focused by an $f/2.3$ off-axis parabola (OAP) onto thin plastic foil targets, thereby generating a plasma. Protons are accelerated in the plasma and propagate away from the foil. The kinetic energy distribution of the protons was measured by two TPSs (TPS15 and TPS45, positioned at 15° and 45° with respect to the laser propagation direction) and a TOF detector (TOF31, positioned at 31°). The spatial proton beam profile was characterized either by an imaged scintillator screen or by a radiochromic film stack (not shown). Laser light transmitted through the target was collected by a ceramic screen.

differences in the focused intensity distribution, due to inherent shot-to-shot fluctuations, can lead to important differences in the target pre-expansion and the subsequent interaction dynamics and may explain the observed variation in maximum proton energy. The best acceleration performance was observed at 0.5%–3% of transmitted laser light, corresponding to the onset of RIT. In this regime, the highest proton energies were achieved in both directions, whereas higher or lower amounts of transmitted light led to weaker acceleration performance. The peak energy of the protons, as measured by the TPS, was $150 \text{ MeV}_{-11}^{+15}$ MeV at 15° and 63 ± 3 MeV at 45° . Shots yielding $>5\%$ transmission showed strongly reduced acceleration performance with maximum proton energies below 25 MeV in both TPS axes. A comparison of the most energetic protons measured in the 15° and 45° directions for varied laser energies E_L is shown in Fig. 2b. Within the investigated range, the maximum proton energies at 45° scaled with $E_L^{1/2}$, while at 15° a linear trend was established. This fundamental difference in energy scaling suggests that the acceleration scheme varied for the different directions.

Figure 3a shows TPS15 readout images (background subtraction applied) for the five most energetic shots. The most notable observation is the spectral constriction of the separated high-energy component in the proton traces.

Figure 3b displays the analysed particle spectra for the corresponding shots. The marker represents the maximum proton energy used in Fig. 2a. The TPS15 spectra (blue lines) feature a low-energy (<40 MeV) exponential and a separated high-energy (≥ 100 MeV) component, whereas the TPS45 spectra (orange lines) consistently only exhibit an exponentially decaying component. TOF measurements with

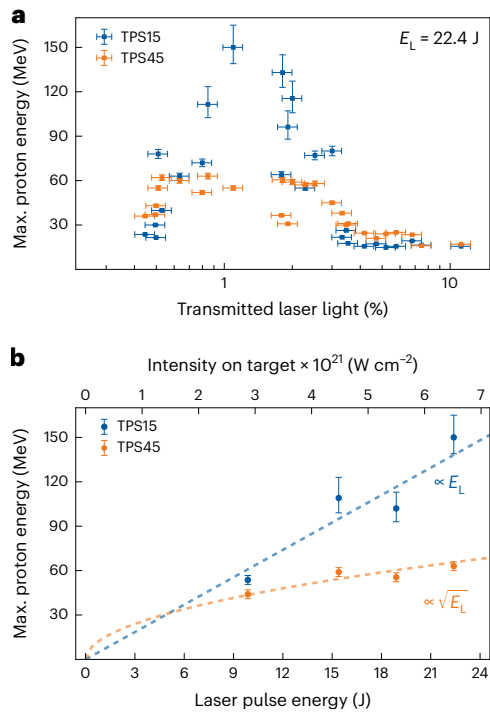


Fig. 2 | Plasma accelerator performance and scalability. **a**, Maximum proton energy from TPS measurements in 15° and 45° directions (TPS15 and TPS45) sorted by transmitted laser light for a total laser pulse energy of $E_L = 22.4$ J. **b**, Maximum proton energies for different laser pulse energies E_L . The upper axis indicates the calculated laser peak intensity. The dotted lines represent proton energy scalings for better trend visualization. The error bars in both panels indicate the systematic uncertainty in maximum energy detection and transmitted light detection, as defined by the detector setup (details in Methods). Max., maximum.

reduced sensitivity at 31° show proton energies exceeding those measured by the TPS45 yet remaining below those observed by the TPS15.

An analysed stack of radiochromic films for a representative high-energy shot is shown in Fig. 3c. The displayed angular dose distribution was derived from lineouts along the horizontal axis covering a vertical angle of 6.5° for each energy layer. The dose maximum of the 35–60 MeV layers of the stack is centred along 45° with a divergence of $\pm 15^\circ$, whereas energy layers >60 MeV show almost no dose in this direction. In contrast, the detected dose at 25° exhibits a clearly reduced divergence of $\pm 3^\circ$ and persists until the last available layer at 104 MeV. The absolute particle spectra in Fig. 3d were derived by deconvoluting the depth-dose profile along the 25° and 45° directions (orange and blue squares). The results are consistent with the TPS measurements.

Figure 3e shows images of the segmented proton beam profiler for the corresponding high-energy shots of Fig. 3a,b. The detected signal behind the 80 and 100 MeV threshold energy absorbers is consistent with the TPS measurements and indicates that the acceleration direction of the most energetic protons is shifted towards the laser propagation direction.

All particle detectors used in the experiment provide consistent evidence that a laser-driven proton beam well exceeding 100 MeV was produced in multiple shots. The proton beam comprises a medium-energy (<70 MeV) broadband component and a spectrally and angularly separated high-energy (>100 MeV) component with reduced divergence. The observed beam parameters and the scaling behaviour of the two components can be associated with multiple acceleration mechanisms. To investigate the cascade of mechanisms matching present laser and target parameters and to identify potential novel aspects, we conducted a combination of hydrodynamic and particle-in-cell simulations. The influence of the preceding laser light on

a 270-nm-thick plastic foil and the resulting expansion was simulated by a two-dimensional hydrodynamic code. The simulation started 100 ps before the laser main pulse arrival, when laser-induced breakdown is known to occur for the target and temporal laser contrast conditions of this experiment^{26,41}. The results of this first simulation stage, ending 1 ps before the laser main pulse, are shown in Supplementary Fig. 1a. The obtained electron density profile was used as input for a subsequent 3D particle-in-cell simulation (details in Methods) investigating the high-intensity interaction. Consideration of the pre-expansion is critical as it leads to a reduction in plasma density towards the onset of RIT for the subsequent main laser pulse (4% transmission in a forward direction). This result is consistent with the findings of our prestudy²⁶, where the onset of RIT was identified at similar values of transmitted laser light and target thickness. Figure 4b shows the simulated angular proton emission distribution in the horizontal plane. The highest proton energies and spectral modulations are observed in the laser propagation direction, whereas protons in the target normal direction show lower energies and an exponentially decaying spectrum, as can be seen from the extracted particle spectra of the different directions in Fig. 4a. To gain deeper insights into the acceleration dynamics during the laser–plasma interaction, a subset of tracer protons was randomly selected upon initialization. The trajectories of these protons were recorded and analysed to understand their individual acceleration based on the respective plasma density and electric field at each simulation time step.

When the relativistic laser pulse penetrates into the expanded plasma, it gets reflected near the relativistically critical density front $n_{cr} = \gamma n_c$. γ is the electron Lorentz factor and n_c the classical critical density, which is defined as $n_c = \epsilon_0 m_e \omega_L^2 / e^2$, with vacuum permittivity ϵ_0 , electron mass m_e , angular laser frequency ω_L and electron charge e . Electrons at n_{cr} are pushed into the target, thereby creating a charge separation field. This field triggers different radiation pressure acceleration (RPA) mechanisms such as hole-boring RPA^{13,19,27}, relativistic transparency front RPA⁴² and collisionless shock acceleration⁴³. For the sake of simplicity, we refer to these acceleration contributions as front surface acceleration (FSA), which is mainly induced by the radiation pressure of the laser and is maintained until the expanding target undergoes RIT.

Throughout the interaction with the plasma, the relativistic laser pulse directly generates electron bunches through the oscillating $j \times B$ term of the Lorentz force^{44–46} and thermal laser absorption mechanisms^{47,48}. The former, prompt electrons^{17,26} are directed primarily in the laser propagation direction and closely follow the oscillating field structure of the laser. In contrast, thermal and recirculating electrons generate a diffuse sheath field at the target rear, which dominates in the target normal direction. The characteristic oscillation of the accelerating field, induced by the prompt electrons, allows distinction between proton acceleration during the interaction with the ultrashort laser pulse at the highest intensity and acceleration within the diffuse non-oscillating sheath field, which can occur on larger spatial and temporal scales.

Protons reaching the highest energies were initially located close to the target front and subjected to a cascade of multiple acceleration mechanisms. To distinguish between these mechanisms, the evolution of the electric field experienced by the tracer particles along their direction of propagation and the target density at their respective positions were studied (Supplementary Information). Figure 4c shows the individual contribution of these distinct mechanisms to the total energy of the fastest protons at the end of the simulation. The time history of the entire acceleration cascade for the most energetic tracer proton is shown in Fig. 4d. In all directions, the fastest protons gain $>50\%$ of their energy from either the prompt or the thermal acceleration phase, in which they were injected with ~ 20 MeV from the FSA phase.

The fastest protons in the 45° direction gain most of their energy within the thermal sheath field, whereas the most energetic protons in the laser propagation direction experience a substantial acceleration contribution due to the field induced by the prompt electron bunches. This field is highest at the rear surface of the target bulk and extends

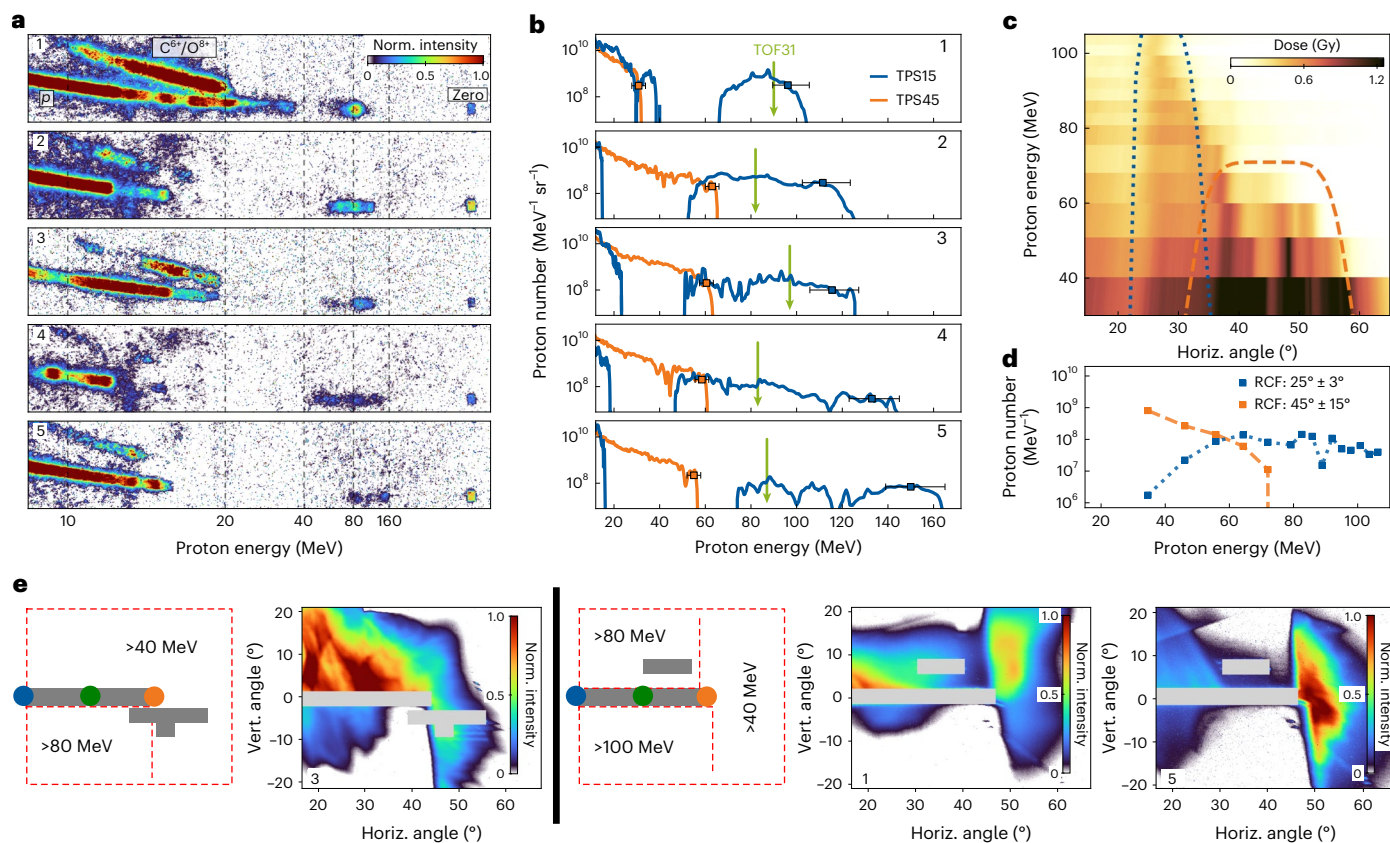


Fig. 3 | Beam parameters for selected high-energy shots. a, TPS15 results (background subtracted and normalized raw images) showing the zero deflection axis (Zero) and parabolic traces from protons (p) and ions (C^{6+}/O^{8+}) for the five most energetic shots (labelled 1–5). **b**, Corresponding particle spectra (solid lines) and maximum energies (squares) for TPS15 and TPS45, with error bars indicating the energy uncertainty as defined by the projected pinhole size (details in Methods). The green arrow displays the maximum energy measured by the TOF in the 31° direction. **c**, Angular dose distribution from radiochromic film (RCF) measurements for a representative high-energy shot. **d**, Particle spectra

generated with the angular areas indicated by the respective dashed/dotted lines in **c**, **e**. Proton beam profiles from scintillator measurements for shots 1, 3 and 5. Two different absorber configurations (sketch) with spatially varying threshold energies (40, 80 and 100 MeV, respectively) were used. There is a clear shift of the acceleration direction of the high-energy protons towards the laser direction (smaller angles). The spectrometers' axes are indicated by coloured circles (TPS15, blue; TOF31, green; TPS45, orange), and grey areas indicate parts without data. Horiz., horizontal; Norm, normalized; Vert., vertical.

throughout the rear-side plasma sheath. Within the first 70 fs after the arrival of the laser main pulse, protons in the rear-side sheath are accelerated by this field in the laser forward direction. Simultaneously, this field prevents electrons from neutralizing the charge of the escaping protons beyond the effective Debye length. The resulting charge separation within the sheath induces an additional ambipolar Coulomb field. This Coulomb field affects the fast protons originating from the front surface, resulting in a momentum spread that further enhances the energy of the fastest particles. We refer to this acceleration contribution as additional Coulomb repulsion (CR). As the prompt electrons generate the highest electron density in the laser propagation direction, CR is particularly relevant for fast protons moving in that direction. These protons gain >25% of their total energy by CR, whereas for protons in the target normal direction, CR is responsible for only 13% of their total energy.

The angular dependent spectral modulations of the proton emission distribution result from the complex interplay of the various mechanisms. Typically, spectral modulations manifest when a part of the proton ensemble traverses field gradients localized in space and time. A detailed analysis of the phase space development in the simulation revealed spectral signatures of each mechanism, which all superimpose to form the spectrally resolved angular distribution in Fig. 4b. This includes monoenergetic features in the RPA phase, an exponential energy distribution due to the expansion phase^{23,24}, ambipolar field structures at the target rear side where carbon ions and protons undergo demixing⁴⁹ as well as strong field gradients during the CR phase^{16,24}.

Despite performing state-of-the-art simulations based on detailed experimental measurements, assigning the present simulation to a specific shot of the experiment requires more precise knowledge of the corresponding interaction parameters and fewer numerical simplifications. This necessitates progress in experimental metrology and an increase in accessible computational resources. Nonetheless, the simulation results replicate the experimental observations for an average good shot, including the angular proton emission distribution, the spectral modulation in the laser propagation direction and the amount of transmitted laser light. Although the observation of multiple acceleration phases is similar to previous research in the RIT regime^{24,27,33}, the fundamental difference of this work is the role of the prompt electrons for ultrashort laser pulses and target densities at the onset of RIT. These prompt electrons facilitate efficient energy transfer from the ultra-intense laser to the protons both during and after the interaction with the laser pulse. The linear scaling of the experimentally observed maximum proton energies at 15° with laser energy can therefore be associated with the dominance of the prompt acceleration in the laser propagation direction¹⁷.

In conclusion, this proof-of-principle achievement to generate spectrally modulated proton beams with maximum energies surpassing 100 MeV marks an important milestone in the field of plasma accelerators, paving the way towards the use of laser-driven ion sources for various demanding applications. Based on the experimental energy scaling, maximum proton energies beyond 250 MeV can be

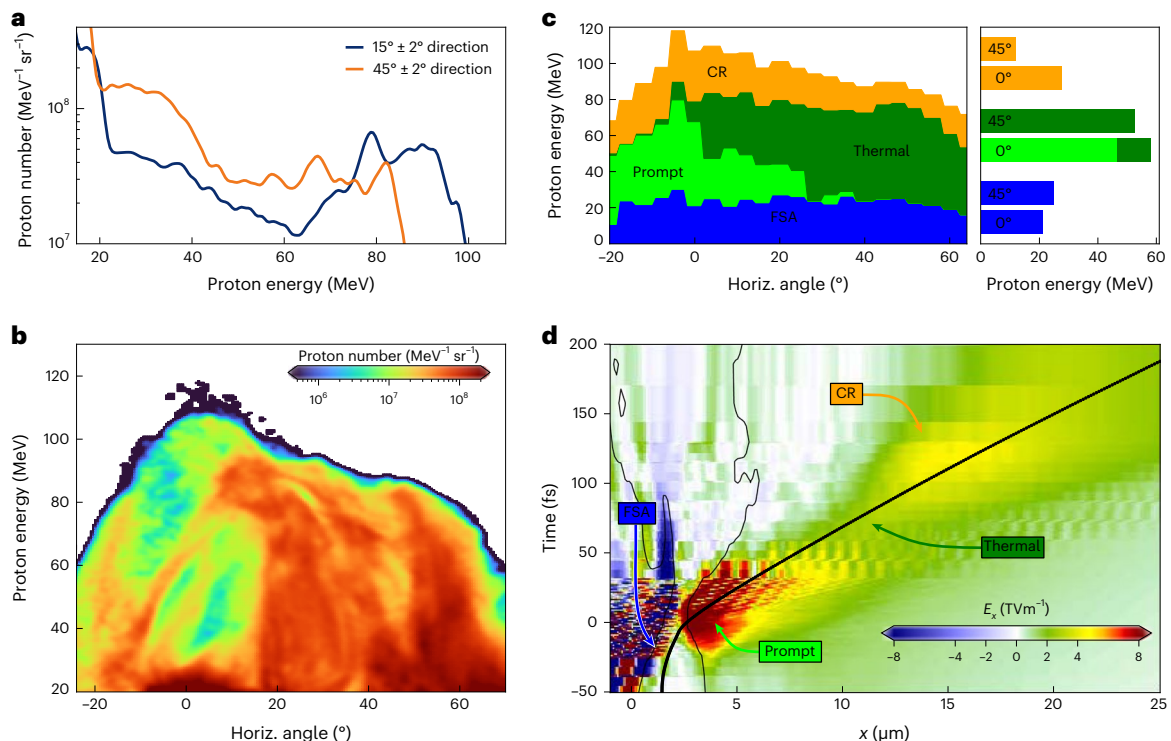


Fig. 4 | Simulation results revealing multiple acceleration contributions in different directions. **a**, Proton energy spectra extracted from 3D particle-in-cell simulation for different spatial directions. **b**, Simulation results of proton emission distribution. Only protons in the central slice of $\pm 1 \mu\text{m}$ around the symmetry plane within a vertical emission range of $\pm 3^\circ$ are shown. **c**, Angularly resolved contribution of different mechanisms to the acceleration cascade of the fastest protons (orange, CR; dark green, thermal, diffuse sheath field set up by thermal and recirculating electrons; light green, prompt, $j \times B$

accelerated electron bunches; blue, FSA, target front and bulk acceleration; see Supplementary Fig. 2 for details). The right panel shows the individual energy contribution of each mechanisms for two selected directions (0° and 45°). **d**, Time history of the electric field E_x along the propagation direction x of the most energetic tracer proton. The trajectory of this proton is depicted by the thick black line. The contour of the relativistically corrected critical density (γn_c) of the target is shown by the thin black line.

extrapolated at twice the laser pulse energy, provided suitable interaction parameters for an efficient cascade of mechanisms are achieved. Target transparency was identified as a simple control parameter for determining the high-performance domain owing to its sensitivity to subtle changes in the initial laser–target conditions. Using the transmitted laser light as an independent feedback parameter related to acceleration performance is ideal for future automated laser and target optimization. Advanced experimental diagnostics involving self-generated and transmitted laser light^{34,50,51}, in conjunction with advanced simulation approaches^{38,52}, can be employed for this purpose. In combination with the relatively high repetition rate ($\geq 1 \text{ Hz}$) of ultrashort pulse lasers, these approaches have the potential to enhance the acceleration stability for practical applications. The ultrashort pulse duration of the laser promotes a rapid succession of multiple acceleration regimes at the highest intensities, as revealed by 3D simulations. The results emphasize the potential of these compact petawatt-class laser systems and interaction parameters to further scale laser-driven ion acceleration to unprecedented energy levels.

Online content

Any methods, additional references, Nature Portfolio reporting summaries, source data, extended data, supplementary information, acknowledgements, peer review information; details of author contributions and competing interests; and statements of data and code availability are available at <https://doi.org/10.1038/s41567-024-02505-0>.

References

- Albert, F. et al. 2020 roadmap on plasma accelerators. *New J. Phys.* **23**, 031101 (2021).
- Daido, H., Nishiuchi, M. & Pirozhkov, A. S. Review of laser-driven ion sources and their applications. *Rep. Prog. Phys.* **75**, 056401 (2012).
- Macchi, A., Borghesi, M. & Passoni, M. Ion acceleration by superintense laser-plasma interaction. *Rev. Mod. Phys.* **85**, 751–793 (2013).
- Kroll, F. et al. Tumour irradiation in mice with a laser-accelerated proton beam. *Nat. Phys.* **18**, 316–322 (2022).
- Busold, S. et al. Shaping laser accelerated ions for future applications—The LIGHT collaboration. *Nucl. Instrum. Methods Phys. Res. A* **740**, 94–98 (2014).
- Aymar, G. et al. LhARA: the laser-hybrid accelerator for radiobiological applications. *Front. Phys.* **8**, 567738 (2020).
- Roth, M. et al. Bright laser-driven neutron source based on the relativistic transparency of solids. *Phys. Rev. Lett.* **110**, 044802 (2013).
- Roth, M. et al. Fast ignition by intense laser-accelerated proton beams. *Phys. Rev. Lett.* **86**, 436–439 (2001).
- Snively, R. A. et al. Intense high-energy proton beams from petawatt-laser irradiation of solids. *Phys. Rev. Lett.* **85**, 2945–2948 (2000).
- Gaillard, S. A. et al. Increased laser-accelerated proton energies via direct laser-light-pressure acceleration of electrons in microcone targets. *Phys. Plasmas* **18**, 056710 (2011).
- Wagner, F. et al. Maximum proton energy above 85 MeV from the relativistic interaction of laser pulses with micrometer thick CH₂ targets. *Phys. Rev. Lett.* **116**, 205002 (2016).
- Fuchs, J. et al. Laser-driven proton scaling laws and new paths towards energy increase. *Nat. Phys.* **2**, 48–54 (2006).

13. Palmer, C. A. J. et al. Monoenergetic proton beams accelerated by a radiation pressure driven shock. *Phys. Rev. Lett.* **106**, 014801 (2011).
14. Haberberger, D. et al. Collisionless shocks in laser-produced plasma generate monoenergetic high-energy proton beams. *Nat. Phys.* **8**, 95–99 (2012).
15. Palaniyappan, S. et al. Efficient quasi-monoenergetic ion beams from laser-driven relativistic plasmas. *Nat. Commun.* **6**, 10170 (2015).
16. Hilz, P. et al. Isolated proton bunch acceleration by a petawatt laser pulse. *Nat. Commun.* **9**, 423 (2018).
17. Zeil, K. et al. Direct observation of prompt pre-thermal laser ion sheath acceleration. *Nat. Commun.* **3**, 874 (2012).
18. McIlvenny, A. et al. Selective ion acceleration by intense radiation pressure. *Phys. Rev. Lett.* **127**, 194801 (2021).
19. Kim, I. J. et al. Radiation pressure acceleration of protons to 93 MeV with circularly polarized petawatt laser pulses. *Phys. Plasmas* **23**, 070701 (2016).
20. Ma, W. J. et al. Laser acceleration of highly energetic carbon ions using a double-layer target composed of slightly underdense plasma and ultrathin foil. *Phys. Rev. Lett.* **122**, 014803 (2019).
21. Ziegler, T. et al. Proton beam quality enhancement by spectral phase control of a PW-class laser system. *Sci. Rep.* **11**, 7338 (2021).
22. Rehwald, M. et al. Ultra-short pulse laser acceleration of protons to 80 MeV from cryogenic hydrogen jets tailored to near-critical density. *Nat. Comm.* **14**, 4009 (2023).
23. Qiao, B. et al. Dominance of radiation pressure in ion acceleration with linearly polarized pulses at intensities of 1021 W/cm². *Phys. Rev. Lett.* **108**, 115002 (2012).
24. Kim, I. J. et al. Transition of proton energy scaling using an ultrathin target irradiated by linearly polarized femtosecond laser pulses. *Phys. Rev. Lett.* **111**, 165003 (2013).
25. Nishiuchi, M. et al. Dynamics of laser-driven heavy-ion acceleration clarified by ion charge states. *Phys. Rev. Res.* **2**, 033081 (2020).
26. Dover, N. P. et al. Enhanced ion acceleration from transparency-driven foils demonstrated at two ultraintense laser facilities. *Light Sci. Appl.* **12**, 71 (2023).
27. Higginson, A. et al. Near-100 MeV protons via a laser-driven transparency-enhanced hybrid acceleration scheme. *Nat. Commun.* **9**, 724 (2018).
28. Thaury, C. et al. Plasma mirrors for ultrahigh-intensity optics. *Nat. Phys.* **3**, 424–429 (2007).
29. Schwoerer, H. et al. Laser-plasma acceleration of quasi-monoenergetic protons from microstructured targets. *Nature* **439**, 445–448 (2006).
30. Hegelich, B. M. et al. Laser acceleration of quasi-monoenergetic MeV ion beams. *Nature* **439**, 441–444 (2006).
31. d’Humières, E., Lefebvre, E., Gremillet, L. & Malka, V. Proton acceleration mechanisms in high-intensity laser interaction with thin foils. *Phys. Plasmas* **12**, 062704 (2005).
32. Yin, L. et al. Monoenergetic and GeV ion acceleration from the laser breakout afterburner using ultrathin targets. *Phys. Plasmas* **14**, 056706 (2007).
33. Henig, A. et al. Enhanced laser-driven ion acceleration in the relativistic transparency regime. *Phys. Rev. Lett.* **103**, 045002 (2009).
34. Palaniyappan, S. et al. Dynamics of relativistic transparency and optical shuttering in expanding overdense plasmas. *Nat. Phys.* **8**, 763–769 (2012).
35. Bin, J. et al. Ion acceleration using relativistic pulse shaping in near-critical-density plasmas. *Phys. Rev. Lett.* **115**, 064801 (2015).
36. Bin, J. et al. Enhanced laser-driven ion acceleration by superponderomotive electrons generated from near-critical-density plasma. *Phys. Rev. Lett.* **120**, 074801 (2018).
37. Mishra, R., Fiuzu, F. & Glenzer, S. Enhanced ion acceleration in transition from opaque to transparent plasmas. *New J. Phys.* **20**, 043047 (2018).
38. Goodman, J., King, M., Wilson, R., Gray, R. J. & McKenna, P. Optimisation of multi-petawatt laser-driven proton acceleration in the relativistic transparency regime. *New J. Phys.* **24**, 053016 (2022).
39. Vshivkov, V. A., Naumova, N. M., Pegoraro, F. & Bulanov, S. V. Nonlinear electrodynamics of the interaction of ultra-intense laser pulses with a thin foil. *Phys. Plasmas* **5**, 2727–2741 (1998).
40. Schramm, U. et al. First results with the novel petawatt laser acceleration facility in Dresden. *J. Phys. Conf. Ser.* **874**, 012028 (2017).
41. Bernert, C. et al. Transient laser-induced breakdown of dielectrics in ultrarelativistic laser-solid interactions. *Phys. Rev. Appl.* **19**, 014070 (2023).
42. Göthel, I. et al. Optimized laser ion acceleration at the relativistic critical density surface. *Plasma Phys. Control. Fusion* **64**, 044010 (2022).
43. Silva, L. O. et al. Proton shock acceleration in laser-plasma interactions. *Phys. Rev. Lett.* **92**, 015002 (2004).
44. Baton, S. et al. Evidence of ultrashort electron bunches in laser-plasma interactions at relativistic intensities. *Phys. Rev. Lett.* **91**, 105001 (2003).
45. Kluge, T. et al. High proton energies from cone targets: electron acceleration mechanisms. *New J. Phys.* **14**, 023038 (2012).
46. Powell, H. et al. Proton acceleration enhanced by a plasma jet in expanding foils undergoing relativistic transparency. *New J. Phys.* **17**, 103033 (2015).
47. White, R. B. & Chen, F. F. Amplification and absorption of electromagnetic waves in overdense plasmas. *Plasma Phys.* **16**, 565–587 (1974).
48. Mulser, P., Bauer, D. & Ruhl, H. Collisionless laser-energy conversion by anharmonic resonance. *Phys. Rev. Lett.* **101**, 225002 (2008).
49. Huebl, A. et al. Spectral control via multi-species effects in pw-class laser-ion acceleration. *Plasma Phys. Control. Fusion* **62**, 124003 (2020).
50. Bagnoud, V. et al. Studying the dynamics of relativistic laser-plasma interaction on thin foils by means of fourier-transform spectral interferometry. *Phys. Rev. Lett.* **118**, 255003 (2017).
51. Williamson, S. et al. Self-referencing spectral interferometric probing of the onset time of relativistic transparency in intense laser-foil interactions. *Phys. Rev. Appl.* **14**, 034018 (2020).
52. Dolier, E. J., King, M., Wilson, R., Gray, R. J. & McKenna, P. Multi-parameter Bayesian optimisation of laser-driven ion acceleration in particle-in-cell simulations. *New J. Phys.* **24**, 073025 (2022).

Publisher’s note Springer Nature remains neutral with regard to jurisdictional claims in published maps and institutional affiliations.

Open Access This article is licensed under a Creative Commons Attribution 4.0 International License, which permits use, sharing, adaptation, distribution and reproduction in any medium or format, as long as you give appropriate credit to the original author(s) and the source, provide a link to the Creative Commons licence, and indicate if changes were made. The images or other third party material in this article are included in the article’s Creative Commons licence, unless indicated otherwise in a credit line to the material. If material is not included in the article’s Creative Commons licence and your intended use is not permitted by statutory regulation or exceeds the permitted use, you will need to obtain permission directly from the copyright holder. To view a copy of this licence, visit <http://creativecommons.org/licenses/by/4.0/>.

© The Author(s) 2024

Methods

Experimental setup

Experiments were performed with the DRACO-PW laser at Helmholtz-Zentrum Dresden-Rossendorf. DRACO-PW is a Ti:Sa laser system (central wavelength: 810 nm) with two chirped pulse amplification stages, providing 30 fs (full-width at half-maximum) laser pulses with a maximum energy of 22.4 J on-target. The temporal pulse contrast was measured to be $<10^{-12}$ at 100 ps and $<10^{-6}$ at 10 ps (details reported in refs. 21,40). Laser pulses (p-polarization) were focused by an $f/2.3$ off-axis parabola to a spot size of 2.5 μm (full-width at half-maximum) containing 32% of the total laser energy, yielding an estimated peak intensity of $6.5 \times 10^{21} \text{ W cm}^{-2}$ ($a_0 \approx 55$). The laser pulses were focussed under oblique incidence (50°) on Formvar plastic foils (C5H8O2, $\rho \approx 1.2 \text{ g cm}^{-3}$, $n_e = 230 n_c$) in a thickness range from $d = 210\text{--}270 \text{ nm}$. Fundamental laser light transmitted through the target was detected by a ceramic screen of size 16 cm \times 16 cm placed $\sim 33 \text{ cm}$ away from the target and imaged onto a bandpass-filtered ($800 \pm 25 \text{ nm}$) and calibrated complementary metal-oxide-semiconductor detector.

Particle diagnostic

Two TPSs positioned at 15° and 45° with respect to the laser axis measured the proton and ion energy spectra. The minimal detectable proton energy of the TPS measurements was 7 MeV. The energy resolution is dominated by the pinhole size (TPS15: 1 mm, TPS45: 0.3 mm) yielding an uncertainty better than $\pm 4\% \mid \pm 10\%$ (compare to the error bars in Fig. 2a,b) for a maximum proton energy of 60 MeV \mid 150 MeV, respectively. Each TPS was equipped with a microchannel plate (MCP) containing a phosphor screen that was imaged onto a charged-coupled device camera. The MCP response up to 60 MeV was cross-calibrated to simultaneous measurements with a calibrated scintillator screen. To avoid any ambiguity in particle species identification, a 3-mm-thick aluminium plate was inserted just in front of the MCP to prevent other ion species from interfering with the detection of the most energetic protons. Scattering contribution induced by the pinhole and the aluminium plate on the energy resolution were calculated to be negligible.

Another particle detection method was realized by TOF measurements. Therefore a high-sensitivity avalanche photodiode (Menlo APD210 Si detector; size 0.5 mm diameter; rise time 500 ps) was placed at a distance of $\sim 4 \text{ m}$ from the target at an angle of 31° with respect to the laser axis. Carbons and heavier ions were blocked by a 2 mm copper plate just in front of the diode (threshold: 34 MeV for protons, 64 MeV u^{-1} for carbons). Signal readout was provided by a fast oscilloscope (Tektronix MSO64, 6 GHz, 25 GSamples per second). Due to the lower sensitivity of this detection method (in comparison to the TPS), the TOF is suitable to confirm the maximum energy level but is unable to derive particle numbers for the most energetic protons.

Spatially resolved particle detection was conducted with a proton beam profiler. A calibrated scintillator (DRZ High from MCI Optonix) of size 100 mm \times 100 mm was positioned at a distance of 87 mm from the target. The emitted luminescence light was captured by a bandpass-filtered ($540 \pm 2 \text{ nm}$) charged-coupled device camera. Separation between protons of different energy is achieved by filtering using absorbers of different thicknesses (absorber thickness, threshold energy: 8 mm Al, 42 MeV protons \mid 78 MeV u^{-1} carbons; 25 mm Al, 80 MeV protons \mid 149 MeV u^{-1} carbons; 38 mm Al, 102 MeV protons \mid 190 MeV u^{-1} carbons). A slit in the central horizontal plane of the scintillator allowed for the parallel operation of the TPS and TOF detectors. For selected shots, a radiochromic film stack was placed 55 mm behind the target, blocking all other particle diagnostics. We used Gafchromic EBT3 films with a size of 100 mm \times 50 mm and a dose range from 0.1 to 20 Gy interleaved with copper plates as absorber material. We derived the angular proton dose distribution from lineouts along the horizontal axis covering a vertical angle of 6.5° for each energy layer.

Numerical simulations

We used two different numerical codes to model the experiment. As a first stage, the FLASH code (v.4.6.2)⁵³ was used in a two-dimensional radially symmetric geometry with adaptive mesh refinement to perform a hydrodynamic simulation of the preceding laser-light-induced expansion of a 270 nm Formvar foil. This simulation covered the time period from the onset of laser-induced dielectric breakdown (around 100 ps) up to 1 ps before the laser main pulse. The breakdown point was derived using the measured laser contrast²¹ and optical probing studies of the laser-induced breakdown of Formvar foils following the approach described in refs. 41,54. The tabulated equation of state was used in the simulations, generated using the FEOS code⁵³. We used the Lee–More conductivity and heat exchange. The resulting density profile from the hydrodynamic simulation, shown in Supplementary Fig. 1, was rotated around its axis of symmetry and used as initial input for a 3D particle-in-cell simulation, with densities below $0.04 n_c$ discarded. The final picosecond and main pulse interaction were modelled using the fully relativistic code PICongPU⁵⁵ (running on 900 A100 graphics processing units for 35,000 timesteps). The laser was focused to a Gaussian spot with $w_0 = 2.14 \mu\text{m}$ on the front surface of the target in p-polarization under oblique incidence (45°) aiming at the centre of the originally unexpanded foil. The temporal intensity profile was matched to measured data from ref. 21 by fitting two exponential ramps and a 30 fs Gaussian with a peak a_0 of about 50. A cell size of 20 nm and one carbon and eight hydrogen macroparticles (thus, 13 electrons) per cell were initialized.

Data availability

All raw data that support the plots within this paper and other findings of this study are available via Rodare (<https://doi.org/10.14278/rodare.2750>) (ref. 56). Source data are provided with this paper.

Code availability

All codes used for this study are available from the corresponding author on reasonable request.

References

53. Fryxell, B. et al. FLASH: an adaptive mesh hydrodynamics code for modeling astrophysical thermonuclear flashes. *Astrophys. J. Suppl. Ser.* **131**, 273–334 (2000).
54. Wang, D. et al. Laser-induced damage thresholds of ultrathin targets and their constraint on laser contrast in laser-driven ion acceleration experiments. *High Power Laser Sci. Eng.* **8**, e41 (2020).
55. Bussmann, M. et al. Radiative signatures of the relativistic Kelvin-Helmholtz instability. In *Proc. International Conference for High Performance Computing, Networking, Storage and Analysis* 1–12 (ACM, 2013); <https://doi.org/10.1145/2503210.2504564>
56. Ziegler, T. et al. Source data: Laser-driven high-energy proton beams from cascaded acceleration regimes. *Rodare*, <https://doi.org/10.14278/rodare.2750> (2024).

Acknowledgements

We thank the DRACO-PW operation team for their experiment support. This work was supported by Laserlab Europe V (PRISES, grant no. 871124) and the IMPULSE project (grant no. 871161). M.N. was supported by JSPS Kakenhi grant nos. 20H00140, 21KK0049 and 22H00121; and QST President's Strategic Grant (QST International Research Initiative (AAA98) and Creative Research (ABACS)).

Author contributions

T.Z., S.A., F.-E.B., L.G., S.K., F.K., J.M.-N., I.P., T.P., M. Rehwald, M. Reimold, H.-P.S., M.E.P.U., M.V. and K.Z. set up and performed the experiment. T.Z. performed the analysis and interpretation of the experimental data with support from F.-E.B., F.K., M. Rehwald,

M.E.P.U. and K.Z. I.G. performed and analysed the numerical simulations with support from N.P.D. and T.K. T.Z., I.G., T.K. and K.Z. interpreted the numerical simulation data. T.Z. and K.Z. wrote the manuscript. U.S. and K.Z. supervised the project. All authors reviewed the manuscript and contributed to discussions.

Funding

Open access funding provided by Helmholtz-Zentrum Dresden - Rossendorf e. V..

Competing interests

The authors declare no competing interests.

Additional information

Supplementary information The online version contains supplementary material available at <https://doi.org/10.1038/s41567-024-02505-0>.

Correspondence and requests for materials should be addressed to Tim Ziegler.

Peer review information *Nature Physics* thanks Igor Andriyash, Jianhui Bin and the other, anonymous, reviewer(s) for their contribution to the peer review of this work.

Reprints and permissions information is available at www.nature.com/reprints.